10/7-21-92 OSTI

SANDIA REPORT

SAND91--0894 • UC--814
Unlimited Release
Printed July 1992

Yucca Mountain Site Characterization Project

Anisotropy of the Topopah Spring Member Tuff

R. J. Martin III, R. H. Price, P. J. Boyd, R. W. Haupt

Prepared by
Sandia National Laboratories
Albuquerque, New Mexico 87185 and Livermore, California 94550
for the United States Department of Energy
under Contract DE-AC04-76DP00789

"Prepared by Yucca Mountain Site Characterization Project (YMSCP) participants as part of the Civilian Radioactive Waste Management Program (CRWM). The YMSCP is managed by the Yucca Mountain Project Office of the U.S. Department of Energy, DOE Field Office, Nevada (DOE/NV). YMSCP work is sponsored by the Office of Geologic Repositories (OGR) of the DOE Office of Civilian Radioactive Waste Management (OCRWM)."

Issued by Sandia National Laboratories, operated for the United States Department of Energy by Sandia Corporation.

Available to DOE and DOE contractors from
Office of Scientific and Technical Information
PO Box 62
Oak Ridge, TN 37831

Prices available from (615) 576-8401, FTS 626-8401

Available to the public from
National Technical Information Service
US Department of Commerce
5285 Port Royal Rd
Springfield, VA 22161

NTIS price codes
Printed copy: A03
Microfiche copy: A01

SAND--91-0894
DE92 017356

SAND91-0894
Unlimited Release
Printed July 1992

ANISOTROPY OF THE TOPOPAH SPRING MEMBER TUFF

R. J. Martin III[†], R. H. Price[‡], P. J. Boyd[†], and R. W. Haupt[†]

[†]New England Research, Inc.
White River Junction, VT 05001

[‡]Geoscience Assessment and Validation Division
Sandia National Laboratories
Albuquerque, New Mexico 87185

ABSTRACT

The mechanical properties of the tuffaceous rocks within Yucca Mountain are needed for near- and far-field modeling of the potential nuclear waste repository. If the mechanical properties are significantly anisotropic (i.e., direction-dependent), a more complex model is required. Relevant data from tuffs tested in earlier studies indicate that elastic and strength properties are anisotropic. This scoping study confirms the elastic anisotropy and concludes some tuffs are transversely isotropic. An approach for sampling and testing the rock to determine the magnitude of the anisotropy is proposed.

This work was performed under the auspices of the U. S. Department of Energy (US DOE), Office of Civilian Radioactive Waste Management, Yucca Mountain Site Characterization Project, under Contract #DE-AC04-76DP00789. The activities described in this document were performed under Work Breakdown Structure (WBS) Element 1.2.3.2.7.1.3.

TABLE OF CONTENTS

CONTENTS (concluded)

ANISOTROPY OF THE TOPOPAH SPRING MEMBER TUFF

1.0 Introduction

Investigations are under way to determine the mechanical, thermal, and petrological properties of rocks in the vicinity of the potential nuclear waste repository at Yucca Mountain, Nevada. While many routine measurements will be carried out, any comprehensive interpretation of these studies requires an analysis of the variation in properties as a function of orientation with respect to the depositional surface. It is important to determine if the rocks exhibit anisotropic properties. If the elastic and thermal constants vary with orientation (i.e., anisotropy), the fracture strength may also vary with direction.

Anisotropy is due to the preferred alignment of microcracks, elliptical pores, or mineral grains. Microcracks develop along grain boundaries as rocks with anisotropic minerals cool and/or depressurize. This occurs either through uplift or cooling in the case of extrusive rocks. Elliptical pores form most frequently due to the compaction of gas-filled cavities as extrusive rocks such as tuff solidify. Many rocks, especially metamorphic gneisses, schists, and slates, have a preferred orientation of minerals because of the way they form. Because many minerals have a tendency to be anisotropic, then so do the rocks which contain them.

Mechanical anisotropy is directly observed by considering the relations between stress and strain as a function of orientation within the rock. In the most general case, the relationship between a specified state of stress, σ_{kl}, and the observed strains, ε_{ij}, for a linear elastic solid is given by

$$\varepsilon_{ij} = S_{ijkl}\ \sigma_{kl}, \tag{1}$$

where S_{ijkl} is the compliance tensor. (A review of tensor notation and the definitions for anisotropic material properties are given in Nye, 1964.) The number of coefficients required to completely describe the deformation of a solid depends on its property symmetry. It is convenient to describe the symmetry of the elements in terms of crystallography. Accordingly, an isotropic material can be defined by the fewest elastic constants, two, and a triclinic by the most, twenty-one. For an isotropic rock or crystal, the two coefficients are the familiar Young's modulus, E, and Poisson's ratio, ν; other elastic moduli (e.g., shear modulus, G) can be calculated from these.

Consider a uniaxial compression experiment on an isotropic rock with the stress applied in the

1-direction of an orthogonal coordinate system. The following equations then hold.

$$\varepsilon_{11} = S_{1111}\,\sigma_{11} = E^{-1}\sigma_{11} \tag{2}$$

$$\varepsilon_{22} = S_{2211}\,\sigma_{11} = -\nu E^{-1}\sigma_{11} \tag{3}$$

$$2(S_{1111} - S_{2211}) = G^{-1} \tag{4}$$

S_{1111} is the slope of the ε_{11} vs σ_{11} curve (with the strain measured parallel to the stress); S_{2211} is the slope of the ε_{22} vs σ_{11} curve (with the strain measured normal to the stress).

The symmetry of many rocks is sufficiently described with two elastic constants; however, in the case of sedimentary rocks with pronounced bedding, metamorphic sequences, and igneous rocks with pronounced layering or fabric, the elastic coefficients will vary with orientation. Such rocks can be analyzed in terms of a hexagonal symmetry. The axis normal to the layering or fabric is the axis of symmetry, the 3-axis; the 1- and 2-directions are in the plane of the bedding. Properties in the bedding plane are independent of orientation. The elastic deformation of a hexagonal elastic solid can be completely described with five independent coefficients, S_{1111}, S_{3333}, S_{1122}, S_{1133}, and S_{1313}. S_{1212} is equal to $2(S_{1111} - S_{1122})$. S_{1111} and S_{3333} are the reciprocal of the Young's moduli in the 1- and 3-directions respectively. Rocks characterized in this way are often termed tranversely isotropic (Lo et al., 1986).

Several experiments can be performed to obtain the five compliances. Uniaxial compression experiments on oriented specimens with loading directions parallel to the 1- and 3-directions will give S_{1111}, S_{3333}, S_{1122}, and S_{1133}; S_{1313} can be determined in a shear or torsional test on an appropriately oriented specimen. In some instances due to limited sample availability, a simple hydrostatic compression experiment can be extremely useful in providing an additional constraint on the measurements or in minimizing the number of specimens required to completely characterize the rock. If the linear compressibilities are measured in the 1- and 3-directions (β_1 and β_3), the following relationships can be used for determining the elastic coefficients.

$$\beta_1 = (S_{1111} + S_{1122} + S_{1133}) \tag{5}$$

$$\beta_3 = (S_{3333} + 2S_{1133}) \tag{6}$$

Alternatively, it is possible to prescribe the strains, ε_{kl}, acting on an elastic solid and observe the stresses, σ_{ij}, that develop. For this case the coefficients that relate stress and strain are the stiffnesses, C_{ijkl}. The general relationship is given by the following equation.

$$\sigma_{ij} = C_{ijkl}\,\varepsilon_{kl} \tag{7}$$

By analogy with the compliance measurements, in a rock with hexagonal symmetry, five elastic coefficients are also required to determine the state of stress due to a prescribed set of strains. It should be noted that, whereas there is a relationship between the compliances and stiffnesses, it is not a term-for-term reciprocity. The exact relation is given by

$$C_{ijkl}\,S_{klmn} = \delta_{im}\delta_{jn}, \tag{8}$$

where δ_{im} and δ_{jn} are Kronecker deltas (see Nye, 1964). For example, in the hexagonal system

$$C_{1111} + C_{1122} = \frac{S_{3333}}{S}, \tag{9}$$

where

$$S = S_{3333}(S_{1111} + S_{1122}) - 2(S_{1133})^2. \tag{10}$$

The stiffnesses can be measured using several methods. First, each coefficient can be determined in conventional deformation experiments. If a specimen of a rock with hexagonal symmetry is deformed in uniaxial strain parallel to the 3-direction, then two of the stiffnesses can be calculated from the following relationships.

$$C_{3333} = \frac{\mathrm{d}\sigma_{33}}{\mathrm{d}\varepsilon_{33}} \tag{11}$$

$$C_{1133} = \frac{\mathrm{d}\sigma_{11}}{\mathrm{d}\varepsilon_{33}} \tag{12}$$

Thus, it is possible to characterize an anisotropic rock with hexagonal symmetry by determining five terms of elastic stiffnesses or compliances or a combination of both.

In addition to deformation experiments at strain amplitudes on the order of 10^{-6} to 10^{-4}, stiffness coefficients in single crystals are computed from the acoustic velocity in a specified direction. For a rock which can be characterized as transversely isotropic, the following relations hold (Lo et al., 1986).

$$C_{1111} = \rho\,{V_{P1}}^2 \tag{13}$$

$$C_{1122} = C_{1111} - 2\rho\,{V_{S1}}^2 \tag{14}$$

$$C_{3333} = \rho\,{V_{P3}}^2 \tag{15}$$

$$C_{1313} = \rho\,{V_{S3}}^2 \tag{16}$$

$$\begin{aligned} C_{1133} \;=\; & -C_{1313} + \{4\rho^2 {V_{P45}}^4 - 2\rho {V_{P45}}^2 (C_{1111} + C_{3333} + 2C_{1313}) + \\ & (C_{1111} + C_{1313})(C_{3333} + C_{1313})\}^{0.5} \end{aligned} \tag{17}$$

In these equations, ρ is the average bulk density, V_{P1} is the compressional wave velocity in the 1-direction, V_{P3} is the compressional wave velocity in the 3-direction, and V_{P45} is the compressional wave velocity along a ray 45° to the 1- and 3-directions. The shear wave velocities are measured in the 1- and 3-directions, V_{S3} and V_{S1}. Note that for V_{S1} both the propagation and vibration directions are in the 1-2 plane.

Previous studies by Olsson and Jones (1980) and Price et al. (1984) have indicated that tuffs from Yucca Mountain exhibit anisotropy in their elastic and strength properties. In light of these findings and the potential importance of anisotropy in evaluating the physical properties of the tuff in the vicinity of the potential repository at Yucca Mountain, a detailed study was initiated on one specimen of welded tuff from the Topopah Spring Member. Static measurements were performed on oriented cores to determine the compliances and stiffnesses. Ultrasonic measurements were conducted during the deformation tests and the dynamic and static elastic coefficients were compared. The objectives were to (1) see if the tuff could be characterized as isotropic or transversely isotropic and (2) compare the results obtained ultrasonically with those collected during static deformation. This result is important because it is much easier to perform acoustic velocity experiments than deformation tests. Consequently, anisotropy can be measured with a benchtop acoustic system and the results used to estimate the azimuthal variation of the mechanical and thermal properties.

2.0 Experiment Procedures

Small oriented cores were prepared from a larger core obtained from a Busted Butte outcrop. The axis of the large core, 10/AE/78, was approximately normal to the bedding plane. Three specimens were prepared with the following orientations: parallel to the core axis, normal to the core axis, and at 45° to the core axis. Figure 1 shows the relative orientation of each specimen with respect to the original core and layering planes within the tuff. A coordinate system is shown on the upper left corner of the diagram; the 3-axis is normal to the plane of the bedding and the 1 and 2 axes are in the plane of the bedding. This reference coordinate system will be used to describe the symmetry elements of the tuff samples. Sample information is provided in Table 1.

TABLE 1. SAMPLE CHARACTERISTICS

FORMATION:	Paintbrush Tuff	Paintbrush Tuff	Paintbrush Tuff
MEMBER:	Topopah Spring	Topopah Spring	Topopah Spring
LOCATION:	Busted Butte	Busted Butte	Busted Butte
SAMPLE:	10/AE/78A	10/AE/78B	10/AE/78C
ORIENTATION:	$\parallel$ to Fabric	$\perp$ to Fabric	45° to Fabric
BULK DENSITY [g/cm^3]:	2.33	2.33	2.28
POROSITY:	0.075	0.075	0.102

Each specimen was ground to a right circular cylinder nominally 2.54 cm in diameter and in length. Specific attention was given to ensure that the ends of the specimen were flat and parallel to within $\pm 1.3 \times 10^{-3}$ cm. The specimens were then vacuum dried for 24 hours at 60°C and the dry bulk density was determined. Ultrasonic velocity measurements were carried out on the dried cores as a function of confining pressure; the experimental procedure is given below. Once the dry measurements were completed, the cores were saturated with water and the grain density of each specimen was determined via the immersion technique. Then the velocity measurements for the saturated condition were conducted as a function of confining pressure. The cores with axes parallel and normal to the bedding were then tested in hydrostatic compression, confined

compression and uniaxial strain while simultaneously measuring the compressional and shear wave velocities parallel to their core axes.

2.1 Ultrasonic Velocity Measurements Under Hydrostatic Pressure

The ultrasonic velocities of the compressional wave (P) and two shear waves (S) with orthogonal polarizations were measured for each core. The propagation direction was parallel to the core axis. After accurately measuring the length of the core, the core was jacketed with polyolefin, heat-shrinkable tubing and positioned between two titanium end pieces containing 1 MHz P and S wave piezoelectric crystals. The sample assembly was inserted into a 200 MPa pressure vessel with a 5.5 cm diameter bore. The confining pressure and pore pressure were manually controlled and the output at each pressure level was measured with Sensotec Model TJE pressure transducers. Hydraulic oil was used as a confining medium, and distilled water was used as a pore fluid. A continuous vacuum was applied to the dry sample during the dry measurements. The velocities were determined at effective pressures of 2.5, 5.0, 7.5, 10, 15, 20, and 25 MPa. Effective pressure is defined as the difference between confining and pore fluid pressure.

The P and S wave velocities of the samples at any pressure were obtained by measuring the one-way travel time of the P or S wave along the core axis and dividing it by the sample length. The source crystal was excited by an electrical pulse generated with a Panametrics 5055 PR pulser-receiver. The signal from the receiver crystal was amplified, high-pass filtered at 0.3 MHz, and fed into a LeCroy 9400 digital oscilloscope. The travel time was measured on the oscilloscope screen with a cursor control that has a resolution of 0.02 microseconds. The travel time for both P and S waves is picked where the waveform amplitude exceeds a threshold voltage that is 1.25% of the peak-to-peak amplitude. This technique yields an accurate, self-consistent data set and eliminates much of the uncertainty associated with picking the arrival time. This is a particular advantage for the shear waves when mode conversions generate signals that arrive earlier than the shear wave. The transit time of the P and S wave through the end pieces is subtracted from the travel time measured on the oscilloscope. The correction is obtained by measuring the travel time through the transducer assembly without a sample.

2.2 Hydrostatic Compression on 10/AE/78B

After the dry and saturated acoustic measurements were completed, sample 10/AE/78B was vacuum dried and instrumented with strain gages. Note that the specimen tended to equilibrate to a laboratory dry condition during the instrumentation procedure. Three strain gages, each Micro-Measurements CEA-06-250UW-120, were epoxied to the sample. One gage was positioned on the

cylindrical surface with its grid aligned parallel to the sample axis. The other gages, mounted on the ends of the cylinder, were oriented at 90° to each other. Electrical leads were soldered to the gages and the instrumented sample was encapsulated with Devcon Flexane 80. The Flexane 80 had a thickness of approximately 0.75 cm and served as a jacket to prevent fluid from penetrating the sample. The specimen was inserted into the pressure vessel and pressurized to 50 MPa. The output of the strain gage bridges was amplified with a Validyne Model BA 172 DC amplifier and measured with a digital voltmeter. The bridge was checked with a shunt resister before and after the experiment.

2.3 Hydrostatic, Compression, and Uniaxial Strain Experiments with Velocities

Hydrostatic compression, confined compression, and uniaxial strain experiments were performed on specimens 10/AE/78A and 10/AE/78B while simultaneously measuring the compressional and shear wave velocities parallel to the core axis. After vacuum drying the specimens for 24 hours at 60°C, they were jacketed with 0.13 mm thick copper. The jackets were then seated to the cores by inserting them in a pressure vessel and pressurizing the system to 20 MPa. The specimens were then instrumented with strain gages epoxied parallel (axial) and normal (radial) to the core axis. The strain gages were Micro- Measurements CEA-06-250UW-120. Next the specimen was secured in an ultrasonic transducer assembly similar to that described above. The sample assembly was then inserted into a 200 MPa pressure vessel mounted in a servo-controlled loading frame.

The servo-controlled loading frame exerted an axial load on the sample column. The force was measured with an external load cell, NER-020-J-86. For these experiments the press was operated in displacement feedback. The confining pressure was generated and maintained with a servo-controlled pressure intensifier. The output of a Sensotec Model Z/108-04 pressure transducer provided the feedback signal. For the hydrostatic compression and confined compression experiments, the feedback signal for the pressure system was obtained from the pressure transducer. For the uniaxial strain experiments, the strain gage sensing the strain normal to the loading axis was used as the feedback signal and the confining pressure was allowed to change to maintain a constant transverse (radial) strain.

All the data were recorded using an IBM/XT-based data acquisition system. The data acquisition program, ACQUIRE, developed at New England Research (NER), was used to collect and store the data.

3.0 Experiment Results

Typical results of the velocity measurements under hydrostatic compression are given in Figures 2 and 3. Figure 2 shows the change in velocity as a function of pressure for the dry specimen, 10/AE/78B. The seismic wave propagation direction is normal to the bedding plane. The compressional wave velocity was 4.653 km/s at room pressure. As the confining pressure was augmented to 25 MPa, the velocity increased only slightly, to 4.662 km/s. This is a relatively small change for such a large change in pressure. The polarized shear waves exhibit nearly the same velocity (S1 = 2.821 km/s; S2 = 2.808 km/s) at room pressure and do not increase significantly with increasing pressure. The fact that the polarized shear wave velocities are virtually identical suggests that there is very little anisotropy within the bedding plane. The results for the same specimen under saturated conditions as a function of effective confining pressure are presented in Table 2. Complete saturation was ensured by maintaining a constant pore pressure of 2.5 MPa. The saturated compressional wave velocity was slightly greater (approximately 2%) than that observed in the dry condition. The polarized shear wave velocities were nearly the same for the two orientations and varied 1% or less from those observed in the dry condition. Both the compressional and shear wave velocities for the saturated condition exhibited the same small pressure dependence that was observed for the dry specimen.

Figure 3 shows the velocity data for the horizontally oriented specimen in a vacuum dry condition. The compressional wave velocity was approximately 4.953 km/s and exhibited virtually no pressure dependence (Table 3). This velocity is about 6% greater than the compressional wave velocity for the vertically oriented specimen (Figure 2). Shear wave velocity anisotropy is evident for waves propagated parallel with the bedding (Figure 3). Shear waves with particle motions perpendicular to the bedding (S2) had velocities approximately 2.2% lower than those with motions parallel to the bedding (S1). As with the vertically oriented core, saturation had only a minimal effect on the velocities; the saturated velocities for 10/AE/78A are listed in Table 3 as a function of effective confining pressure, although the shear wave anisotropy increased slightly to 2.6%.

Sample 10/AE/78C is oriented at 45° to the bedding plane. The particle motion of S2 is perpendicular to the trace of the bedding planes, whereas the particle motion of S1 is parallel to the trace of the bedding planes. Measurements for this orientation are necessary to characterize the anisotropy tensor for the tuff. The results of the vacuum dry and water saturated velocity measurements are presented in Table 4 as a function of effective confining pressure; velocity changes with saturation and increasing pressure are similar to those described for the other orientations.

TABLE 2. VELOCITY DATA FOR SAMPLE 10/AE/78B

VACUUM DRY

$(P_c)_e$ [MPa]	P-Wave [km/s]	S1-Wave [km/s]	S2-Wave [km/s]
0.0	4.653	2.821	2.808
2.5	4.662	2.821	2.808
5.0	4.662	2.821	2.808
7.5	4.662	2.824	2.812
10.0	4.662	2.827	2.815
15.0	4.662	2.834	2.818
20.0	4.662	2.834	2.818
25.0	4.662	2.834	2.821

WATER SATURATED; PORE PRESSURE = 2.5 MPa

$(P_c)_e$ [MPa]	P-Wave [km/s]	S1-Wave [km/s]	S2-Wave [km/s]
0.0	4.749	2.808	2.778
2.5	4.749	2.808	2.784
5.0	4.749	2.808	2.787
7.5	4.758	2.808	2.790
10.0	4.767	2.808	2.790
15.0	4.767	2.808	2.787
20.0	4.767	2.808	2.790
25.0	4.767	2.812	2.793

TABLE 3. VELOCITY DATA FOR SAMPLE 10/AE/78A

VACUUM DRY

$(P_c)_e$ [MPa]	P-Wave [km/s]	S1-Wave [km/s]	S2-Wave [km/s]
0.0	4.953	2.945	2.882
2.5	4.953	2.952	2.885
5.0	4.953	2.952	2.885
7.5	4.953	2.956	2.888
10.0	4.953	2.956	2.888
15.0	4.963	2.956	2.892
20.0	4.963	2.966	2.895
25.0	4.973	2.966	2.895

WATER SATURATED; PORE PRESSURE = 2.5 MPa

$(P_c)_e$ [MPa]	P-Wave [km/s]	S1-Wave [km/s]	S2-Wave [km/s]
0.0	4.963	2.922	2.846
2.5	4.963	2.925	2.849
5.0	4.963	2.928	2.853
7.5	4.973	2.928	2.856
10.0	4.973	2.928	2.856
15.0	4.992	2.928	2.856
20.0	4.992	2.932	2.856
25.0	4.992	2.932	2.859

TABLE 4. VELOCITY DATA FOR SAMPLE 10/AE/78C

VACUUM DRY

$(P_c)_e$ [MPa]	P-Wave [km/s]	S1-Wave [km/s]	S2-Wave [km/s]
0.0	4.636	2.793	2.790
2.5	4.653	2.793	2.790
5.0	4.653	2.796	2.790
7.5	4.653	2.796	2.793
10.0	4.662	2.802	2.799
15.0	4.662	2.802	2.802
20.0	4.662	2.805	2.805
25.0	4.662	2.808	2.812

WATER SATURATED; PORE PRESSURE = 2.5 MPa

$(P_c)_e$ [MPa]	P-Wave [km/s]	S1-Wave [km/s]	S2-Wave [km/s]
0.0	4.705	2.721	2.739
2.5	4.705	2.721	2.742
5.0	4.723	2.721	2.745
7.5	4.723	2.721	2.748
10.0	4.723	2.721	2.751
15.0	4.723	2.721	2.751
20.0	4.723	2.727	2.754
25.0	4.723	2.730	2.757

In order to compare the elastic coefficients for tuff calculated from the velocity data with those obtained from static measurements, hydrostatic compression, confined compression, and uniaxial strain experiments were performed on dry tuff specimens. Figure 4 shows the results of the hydrostatic compression experiment for specimen 10/AE/78B; the core axis for this specimen was normal to the apparent bedding. Three strains are plotted as a function of pressure: normal to the layering (the 3-direction) and parallel to the plane of the bedding (the 1- and 2-directions). The greatest strain is observed normal to the bedding. Parallel to the bedding plane, the strains, measured with two orthogonal gages, were smaller than the axial strain; the gages yielded very similar strains at each observation level. The slope of the strain versus pressure curve in a given direction gives the linear compressibility in that direction. The linear compressibilities in the 3- and 1- directions were as follows.

$$\beta_3 = 1.627 \times 10^{-2}\ \mathrm{GPa}^{-1} \tag{18}$$

$$\beta_1 = 1.356 \times 10^{-5}\ \mathrm{GPa}^{-1} \tag{19}$$

The difference in the linear compressibilities is 20%. This is much greater than the anisotropy determined acoustically. Furthermore, the changes in all three strains with confining pressure were nearly linear, meaning the compressibilities were independent of pressure. Each pressure versus strain curve exhibits a small curvature below 10 MPa. The non-linearity is most noticeable in the 1- and 2-directions. This nearly independent behavior with pressure is consistent with the velocity measurements, which also showed no change in velocity with confining pressure.

In order to completely determine the compliances for the specimen, several nonhydrostatic experiments were carried out. Confined compression tests were performed on 10/AE/78A and 10/AE/78B at a fixed confining pressure of 20 MPa. The results of the run on 10/AE/78B are shown in Figure 5, with stress plotted as a function of strain (σ_{33} and ε_{33}). The slope of the curve is ${S_{3333}}^{-1}$. The slope of the transverse strain, ε_{11}, vs longitudinal strain, ε_{33}, is ${S_{1133}}^{-1}$. The results of these calculations, as well as those for the related experiments on 10/AE/78A, are presented in Table 6.

Finally, it seemed worthwhile to directly measure the stiffnesses of the specimens by conducting several uniaxial strain experiments. The results of a typical cyclic load for 10/AE/78B are shown in Figures 6 and 7. The axial stress, σ_{33}, and the radial stress (or confining pressure), σ_{11}, are plotted as a function of axial strain, ε_{33}, in Figures 6 and 7, respectively. For these tests ε_{11} is held constant and equal to zero. The slope of the σ_{33} vs ε_{33} loading curve yields C_{3333}; the slope of the σ_{11} vs ε_{33} curve yields C_{1133}. The stiffnesses for this data set were computed at a mean stress of 20 MPa; the values are presented in Table 6.

TABLE 5. ELASTIC COEFFICIENTS FOR SAMPLE 10/AE/78A

	S_{1111} GPa^{-1}	β_1 GPa^{-1}	C_{1111} GPa	C_{1122} GPa
Static:	0.0185	0.0136	53.90	12.66
Dynamic:			57.21	15.79

TABLE 6. ELASTIC COEFFICIENTS FOR SAMPLE 10/AE/78B

	S_{3333} GPa^{-1}	S_{1122} GPa^{-1}	S_{1133} GPa^{-1}	β_3 GPa^{-1}	C_{3333} GPa	C_{1133} GPa	C_{1313} GPa
Static:	0.0148	-0.0057	-0.0017	0.0163	53.53	15.37	-
Dynamic:					50.89	9.30	19.00

Table 7 presents the static and dynamic elastic constants in terms of the more commonly used engineering constants, Young's modulus, Poisson's ratio, and bulk modulus. Two Young's moduli are calculated; normal to the layering (the 3-direction) and in the plane of the bedding (the 1-direction). Three Poisson's ratios are given (Lo et al., 1986):

$$\nu_1 = \frac{d\varepsilon_{11}}{d\varepsilon_{22}} \tag{20}$$

$$\nu_2 = \frac{d\varepsilon_{33}}{d\varepsilon_{11}} \tag{21}$$

$$\nu_3 = \frac{d\varepsilon_{33}}{d\varepsilon_{11}} \tag{22}$$

TABLE 7. ENGINEERING ELASTIC COEFFICIENTS

	Young's Modulus [GPa]		Bulk Modulus [GPa]	Poisson's Ratio		
	3-direction	1-direction		ν_1	ν_2	ν_3
Static:	46.43	48.11	23.09	0.167	0.239	0.231
Dynamic:	44.42	50.20	28.62	0.212	0.238	0.211

Before proceeding, several additional observations must be mentioned. Hydrostatic compression tests were run on the copper jacketed specimens prior to the deformational experiments. Four observations are pertinent.

(i) The volume compressibilities for both specimens (10AE78A and 10AE78B) were nearly identical.

(ii) The velocities measured on the copper jacketed specimens in the deformational apparatus were identical to those collected in the vacuum dry condition using the hydrostatic, velocity measuring system.

(iii) The volume compressibility for the copper jacketed specimen was 3.628×10^{-2} GPa^{-1}, whereas the volume compressibility for the specimen jacketed in Flexane was 4.305×10^{-2} GPa^{-1}.

(iv) The dynamic stiffnesses calculated from the velocities measured in the uniaxial strain experiments were in excellent agreement with those computed from the velocities collected under hydrostatic pressure; the differences were less than 0.5%.

4.0 Discussion and Conclusions

The experimental data for the Topopah Spring Member welded tuff samples include ultrasonic compressional and shear wave velocities as a function of sample orientation, saturation, pressure, and differential stress (confined compression and uniaxial strain tests). The effects of sample anisotropy are apparent in these measurements. Specifically, the tuff is significantly more compliant normal to the layering than within the bedding plane.

The velocity data indicate that the anisotropy, although small, is consistent with a physically intuitive model in which the welding and compaction process has caused the tuff to become transversely isotropic. The axis of symmetry is perpendicular to the prefferred orientation of the shard matrix, which is the result of gravity and flow during deposition of the ash flow tuff (Price et al., 1985; 1987). Consequently, this prefferred orientation of the shard matrix and, possibly, the pore distribution produced the anisotropy.

For an ideal transversely isotropic material, four relationships hold.

(i) The axis of symmetry is normal to the bedding plane. This is the slow direction for P waves, that is, the minimum velocity. Furthermore, S waves propagating parallel to the axis of symmetry have the same velocity regardless of their vibration direction (particle motion).

(ii) For propagation directions normal to the axis of symmetry (parallel to the bedding plane), P wave velocities are a maximum. Shear waves with a particle motion parallel to the bedding plane have a greater velocity than those with a particle motion perpendicular to the bedding.

(iii) For propagation directions between the two principal directions, the velocities for P waves and S waves with particle motion parallel to the trace of the bedding are intermediate to those observed along the principal directions.

(iv) The velocity of shear waves with a component of particle motion parallel to the axis of symmetry may be either higher or lower than the velocity perpendicular to the axis of symmetry.

Because the pressure dependence of velocity is relatively small, the degree of anisotropy can be described by referring to the velocities measured at low pressure. The P wave velocities in the two samples oriented in the vertical and horizontal direction differ by approximately 0.300 km/s for the dry samples, or about 6.4%. The slow direction for the P wave is parallel with the axis

of symmetry, which is parallel with the axis of the vertically oriented sample, 10/AE/78B. The greatest S wave anisotropy is perpendicular to the axis of symmetry. In this direction the two S waves differ by approximately 0.063 km/s for the dry sample, or about 2.2%. The S wave with the particle motion perpendicular to the axis of symmetry (S1) is faster than that with the particle motion parallel with the axis of symmetry (S2).

Although these velocities are consistent with a transversely isotropic model, sample variability in this limited selection of cores is also apparent. Ideally, the P wave velocities propagated at 45° are intermediate between those parallel and perpendicular to the axis of symmetry. In the data collected for the core oriented at 45°, however, this direction has the lowest P wave velocities. The lowest S wave velocities of either polarization were also recorded for this sample. In addition, this sample has the lowest measured bulk density and highest porosity. A reasonable explanation is that the large core from which these smaller oriented samples were prepared was not homogeneous. Therefore, variability should be averaged out with measurements on a larger set of cores of this size or else larger core sizes.

As discussed in Section 1.0, to completely characterize the elastic behavior of a rock or a crystal with hexagonal symmetry, five coefficients must be determined. For the welded tuff in the dry condition at 20.0 MPa, the five compliance coefficients computed from the velocity data are as follows.

$$C_{1111} = 57.3 \times 10^5 \text{ GPa} \tag{23}$$

$$C_{3333} = 50.6 \times 10^5 \text{ GPa} \tag{24}$$

$$C_{1122} = 16.8 \times 10^5 \text{ GPa} \tag{25}$$

$$C_{1313} = 18.5 \times 10^5 \text{ GPa} \tag{26}$$

$$C_{1133} = 9.3 \times 10^5 \text{ GPa} \tag{27}$$

These values are based on a limited set of velocity measurements. C_{1133}, which is based in part on the suspect P wave velocity measured in the 45° direction, needs further measurements.

Typically the velocities measured in rocks increase with confining pressure. For the tuff samples, however, the pressure dependence of velocity is very small. Over the 25 MPa range of pressure, the largest increase in P wave velocity is 0.03 km/s for the water saturated horizontal sample, or about 0.58%. Similarly, for the S wave the largest increase is 0.021 km/s for the S1 wave in the dry horizontal sample, or about 0.71%. In addition to, at most, a small pressure dependence, the increase in velocity with pressure is approximately linear. This indicates that very little of the total porosity is in the form of compliant cracks, which would give rise to large,

nonlinear increases in velocities as a function of pressure. During the welding and compaction process, all of the cracks and grain contacts were closed and cemented by the flow of the matrix, the vapor phase activity and diffusion through the matrix, and the deposition of tridymite (Price et al., 1985). In addition, the devitrification process did not create new low-aspect-ratio voids (Price et al., 1985; 1987).

The effects of water saturation on velocity in these samples are consistent with the interpretation of a largely noncompliant porosity. Typically, the introduction of water into the pore space increases the overall bulk modulus while having a much smaller effect on the shear modulus. Consequently, P wave velocities increase upon saturation, and a greater increase is observed when porosity is contained in fine, compliant, crack-like pore shapes (Cheng, 1978). The S wave velocities decrease with increasing water saturation and crack concentration. If all of the porosity is perfectly spherical, the bulk and shear moduli are independent of water saturation (as if the pores were not even there). Thus, the P wave and S wave velocities decrease in proportion to the increase in density when going from the dry to saturated condition. For the welded tuff the majority of the porosity is most likely spherical. The saturated S wave velocities are lower than dry, and the decrease is nearly predicted by the increase in water-saturated density. The saturated P wave velocities are equal to or slightly higher than dry, indicating a pore population somewhat less than spherical. Applying the model developed by Cheng (1978), the porosity can be modelled with a distribution of pore shapes with aspect ratios of between 1.0 (spheres) and 0.1 (oblate spheroids).

There is one observation in the dry and saturated data that indicates that the long axis of the oblate spheroidal or tabular pores have a preferred orientation parallel with the lineation or bedding. The effects of saturation are greatest on P wave velocities in the vertical direction. In going from a dry to a saturated condition, P wave velocities increase by 0.096 km/s or about 2.06%. This is not a large increase, but is consistent with a preferred orientation parallel to bedding. In the horizontal direction the increase is only 0.01 km/s, or 0.2%, while at 45° the increase is 0.07 km/s, or about 1.49%. This is also what would be anticipated with a transversely isotropic model, and indicates that at least some of the anisotropy is due to the preferred orientation of pores.

The anisotropy of the welded tuff is also apparent in the linear compressibility data. The linear compressibility, β_3, is approximately 20% greater parallel to the symmetry axis than perpendicular to the symmetry axis, β_1. Furthermore, the two linear compressibilities measured in the bedding plane agree very closely. Therefore, the strain measurements are consistent with a transversely isotropic material. The strain dependence on pressure is nearly linear in all directions, indicating

that the majority of the porosity is not in the form of low-aspect-ratio pores, which would cause a nonlinear behavior at low pressures. In the 3-direction, the strain is larger either because of the preferred orientation of pores parallel with the lineation, or due to the anisotropy and preferred orientation of the mineralogy.

While the linear compressibility data are consistent with a transversely isotropic rock, the two measurements are not sufficient to fully describe the material. For this reason, additional experiments were performed in confined compression and uniaxial strain. The results of these measurements are compiled in Tables 5, 6, and 7. Specifically, it is possible to compare the static and dynamic stiffnesses and engineering elastic constants. The coefficients C_{1111} and C_{1122} are in good agreement for the static and dynamic measurements. The dynamic moduli are somewhat greater than the static. The strain amplitude of static measurements is three to five orders of magnitude larger than dynamic measurements. This static-to-dynamic ratio is in good agreement with previous results (Simmons and Brace, 1965; Cheng and Johnston, 1981). The more crack-like porosity in the sample, the greater is the static-to-dynamic ratio. As pressure increases, the crack porosity decreases and the two compressibilities tend to converge. There was no convergence at higher pressures, and this reinforces the interpretation of oblate rather than crack-like porosity.

A problem arises for C_{3333} and C_{1133}. In both instances, the static coefficients exceed the dynamic. Given the magnitude of the difference, it is well outside the bounds of normal experimental error and directly contradicts the linear compressibility data presented in Figure 4. The measurements were repeated and all the calibrations checked. The result was unchanged. The error apparently resides in the test geometry. The samples were 2.54 cm in both length and diameter. It appears that the impedance contrast between the titanium transducers and the rock altered the strain field near the interface. This effect has been noted by others (e.g., S. R. Brown, personal communication). Furthermore, due to the short sample length, the size of the strain gage grid, and the position of the gages on this particular specimen, the strains have been underestimated. This leads to an overestimation of the stiffnesses. There is no immediate explanation as to why the data on specimen 10/AE/78A yielded consistent results as did 10/AE/78B when they were tested in true hydrostatic compression. The results cannot be attributed to a change in the sample due to multiple loading cycles, because the velocities remained unchanged throughout the sample history. The discrepancy is also reflected in the Young's modulus in the 3-direction; the static modulus exceeds the dynamic. The results indicate that a greater length-to-diameter ratio is necessary for these measurements. The commonly accepted ratio of length-to-diameter is 2.0 to 2.2 to avoid significant end effects.

The results of the study on this specimen of welded tuff clearly indicate that the rock is anisotropic and its elastic behavior can be adequately characterized with five coefficients. The anisotropy of the welded tuff is apparent in the ultrasonic velocity and strain measurements. The source of the anisotropy is either a preferred distribution of ellipsoidal and tabular pores parallel with the lineation or else a preferred distribution of the mineralogy. The degree of anisotropy is on the order of 7% or less in velocity and 20% from the linear compressibilities. Because there is apparently a fair degree of sample inhomogeneity additional measurements on a larger set of samples would be necessary for a complete characterization.

5.0 References

Cheng, C. H., 1978

Seismic Velocities in Porous Rocks: Direct and Inverse Problems, Ph.D. thesis, M.I.T., Cambridge. (NNA.911007.0004)

Cheng, C. H., and D. H. Johnston, 1981

Dynamic and Static Moduli, Geophys. Res. Letters, **8**, 39-42. (NNA.910923.0006)

Lo, T., K. B. Coyner, and M. N. Toksoz, 1986

Experimental Determination of Elastic Anisotropy of Berea Sandstone, Chicopee Shale, and Chelmsford Granite, Geophysics, **51**, 164-171. (NNA.910306.0117)

Nye, J. F., 1985

Physical Properties of Crystals, The University Press, Oxford. (NNA.911021.0031)

Olsson, W. A., and A. K. Jones, 1980

Rock Mechanics Properties of Volcanic Tuffs from the Nevada Test Site, SAND80-1453, Sandia National Laboratories, Albuquerque, NM. (NNA.870406.0497)

Price, R. H., J. R. Connolly, and K. Keil, 1987

Petrologic and Mechanical Properties of Outcrop Samples of the Welded, Devitrified Topopah Spring Member of the Paintbrush Tuff, SAND86-1131, Sandia National Laboratories, Albuquerque, NM. (HQS.880517.1704)

Price, R. H., F. B. Nimick, J. R. Connolly, K. Keil, B. M. Schwartz, and S. J. Spence, 1985

Preliminary Characterization of the Petrologic, Bulk, and Mechanical Properties of a Lithophysal Zone Within the Topopah Spring Member of the Paintbrush Tuff, SAND84-0860, Sandia National Laboratories, Albuquerque, NM. (NNA.870406.0156)

Price, R. H., S. J. Spence, and A. K. Jones, 1984

Uniaxial Compression Test Series on Topopah Spring Tuff from USW GU-3, Yucca Mountain, Nevada Test Site, SAND83-1646, Sandia National Laboratories, Albuquerque, NM. (NNA.870406.0252)

Simmons, G., and W. F. Brace, 1965

Comparison of Static and Dynamic Measurements of Compressibility of Rocks, J. Geophys. Res., **70**, 5649-5656. (NNA.910923.0007)

6.0 Figures

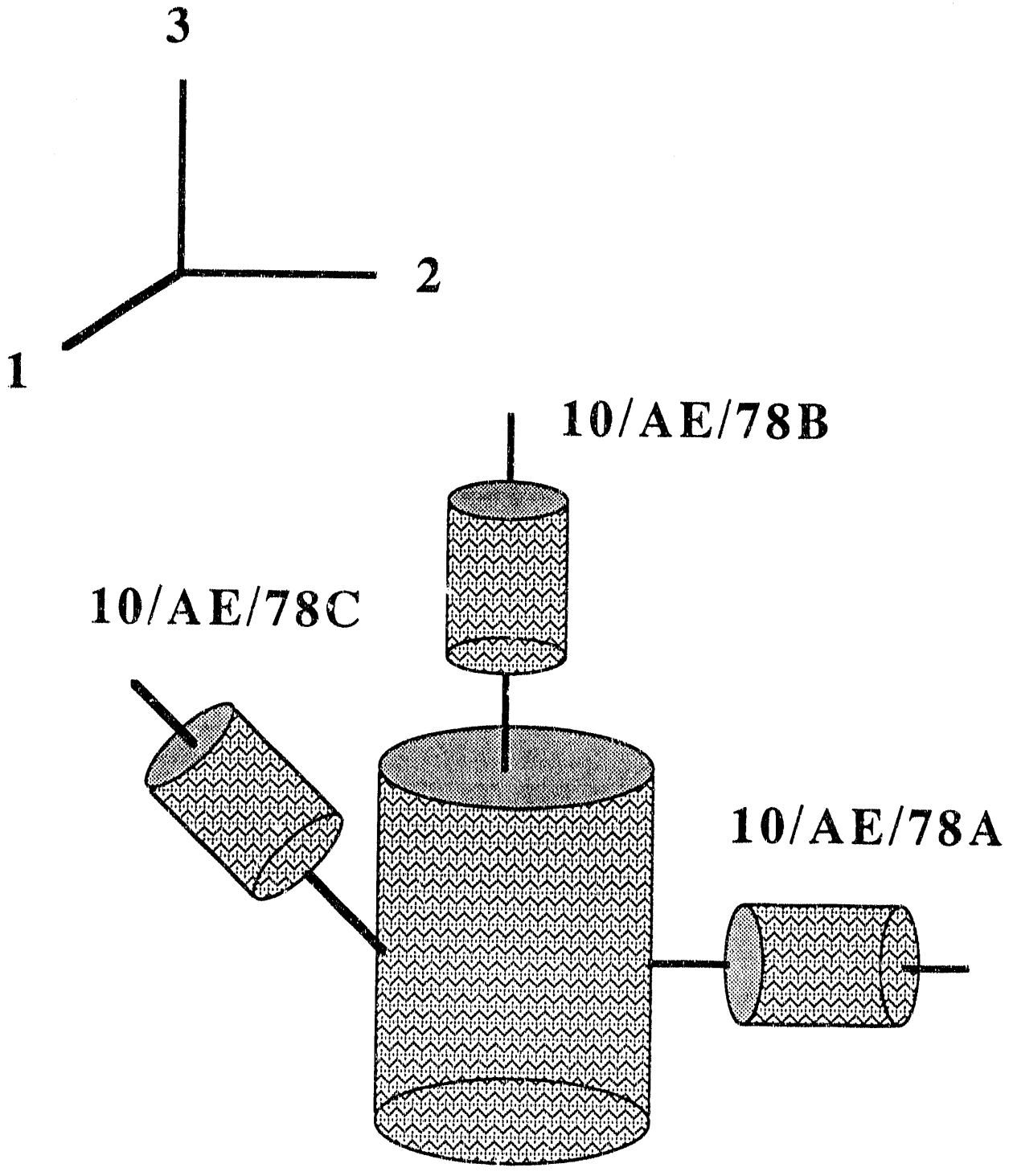

Figure 1. Schematic diagram of the sub-core orientations and designations for the three specimens obtained from Topopah Spring Member welded tuff specimen 10/AE/78. The reference coordinate system used in the discussion is shown in the upper left corner.

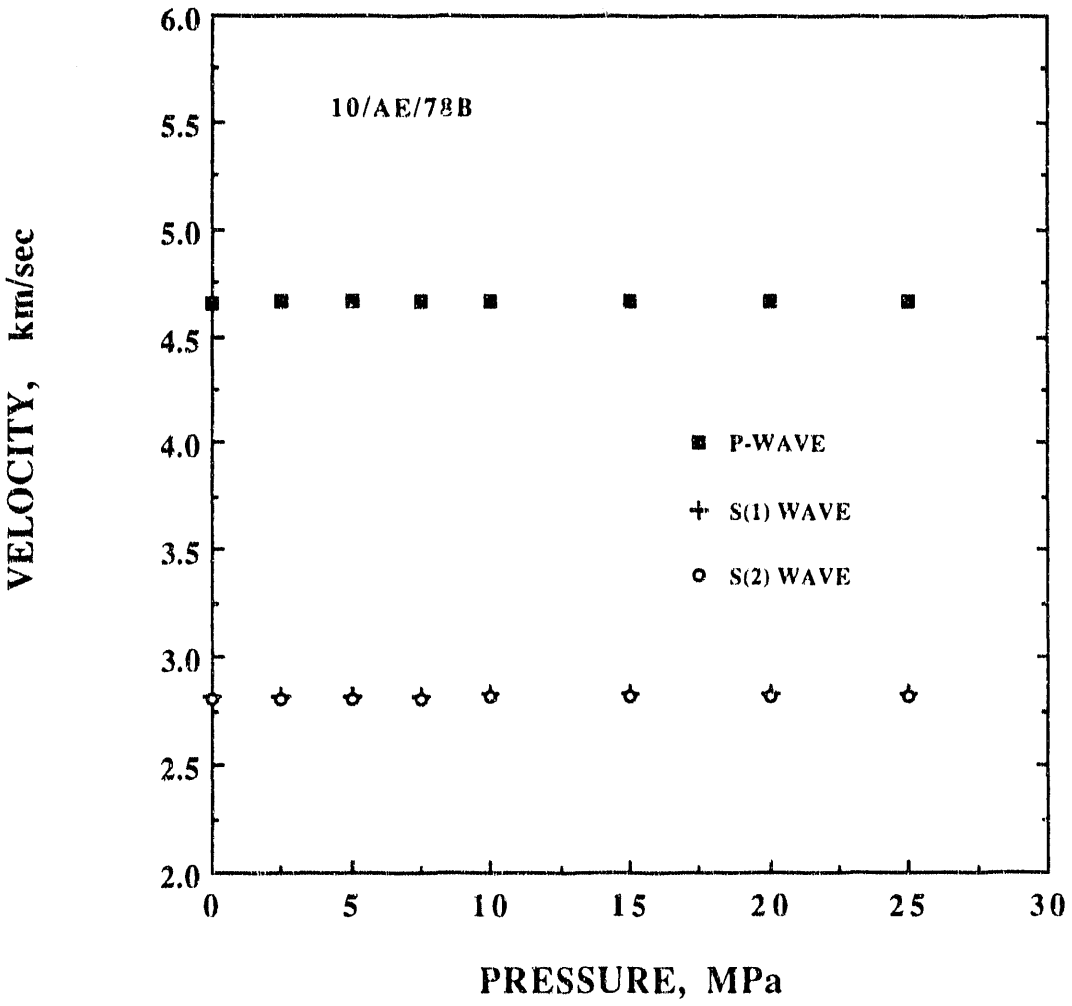

Figure 2. Compressional (P-wave) and shear wave (S1 and S2) velocities are plotted as a function of confining pressure for a vacuum dry specimen of Topopah Spring Member tuff. The propagation direction is parallel to the axis of symmetry (i.e. normal to the bedding plane).

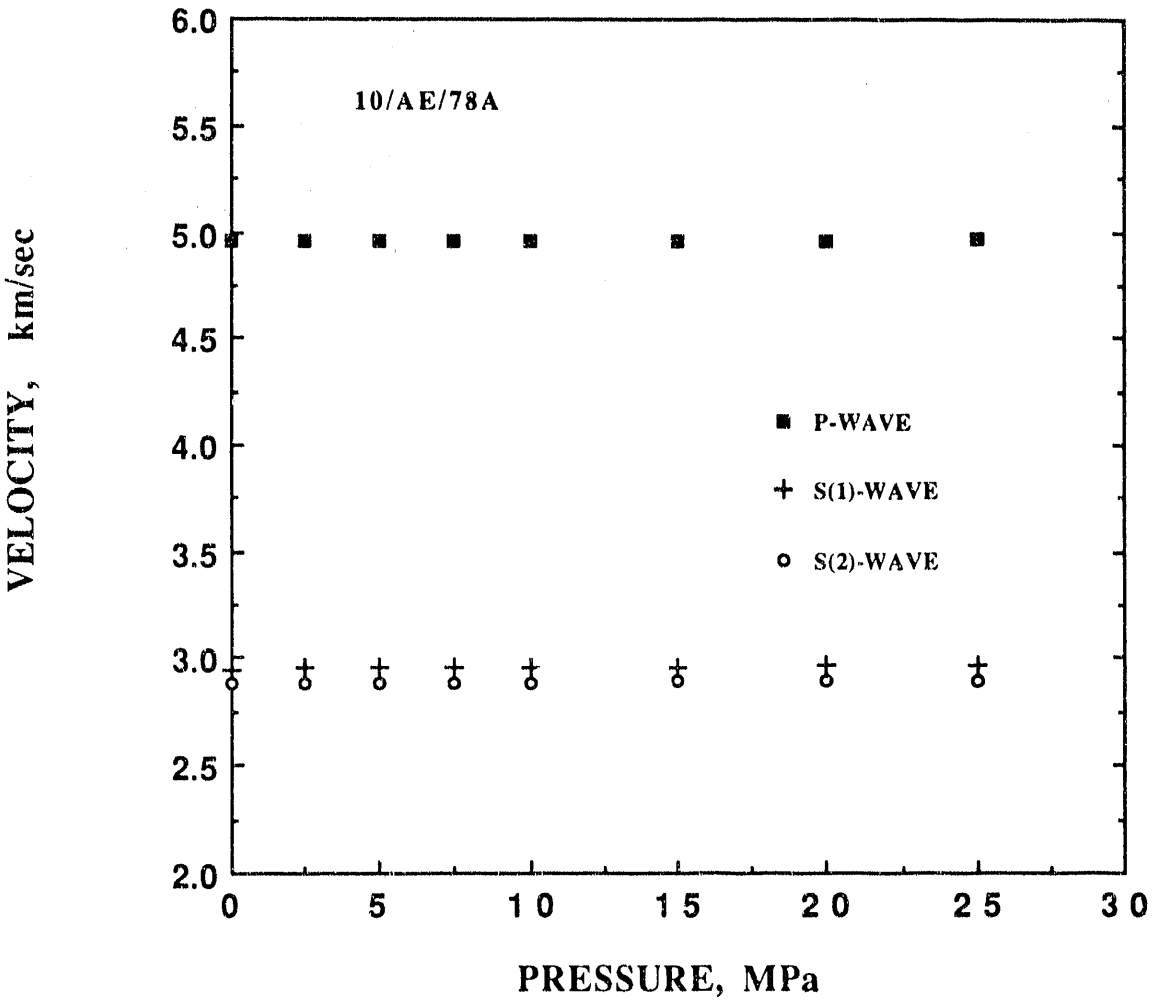

Figure 3. Compressional (P-wave) and shear wave (S1 and S2) velocities are plotted as a function of confining pressure for a vacuum dry specimen of Topopah Spring Member tuff. The propagation direction is parallel to the bedding plane. S1 has a particle motion in the bedding plane; S2 has a particle motion normal to the bedding plane.

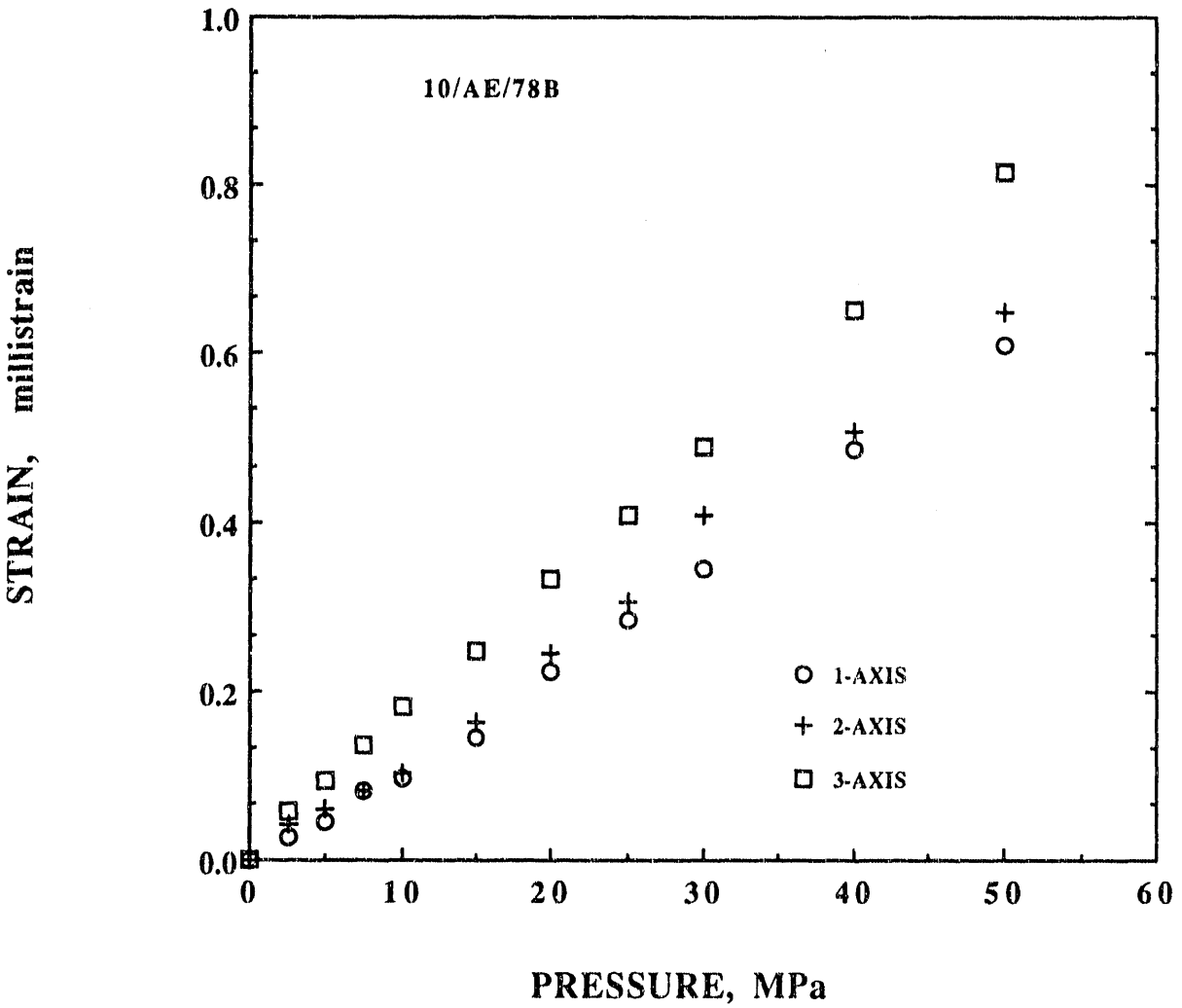

Figure 4. Strains parallel to the 1-, 2-, and 3- directions of Topopah Spring Member tuff specimen 10/AE/78 are plotted as a function of confining pressure. The relation between layering and the coordinate system is shown in Figure 1.

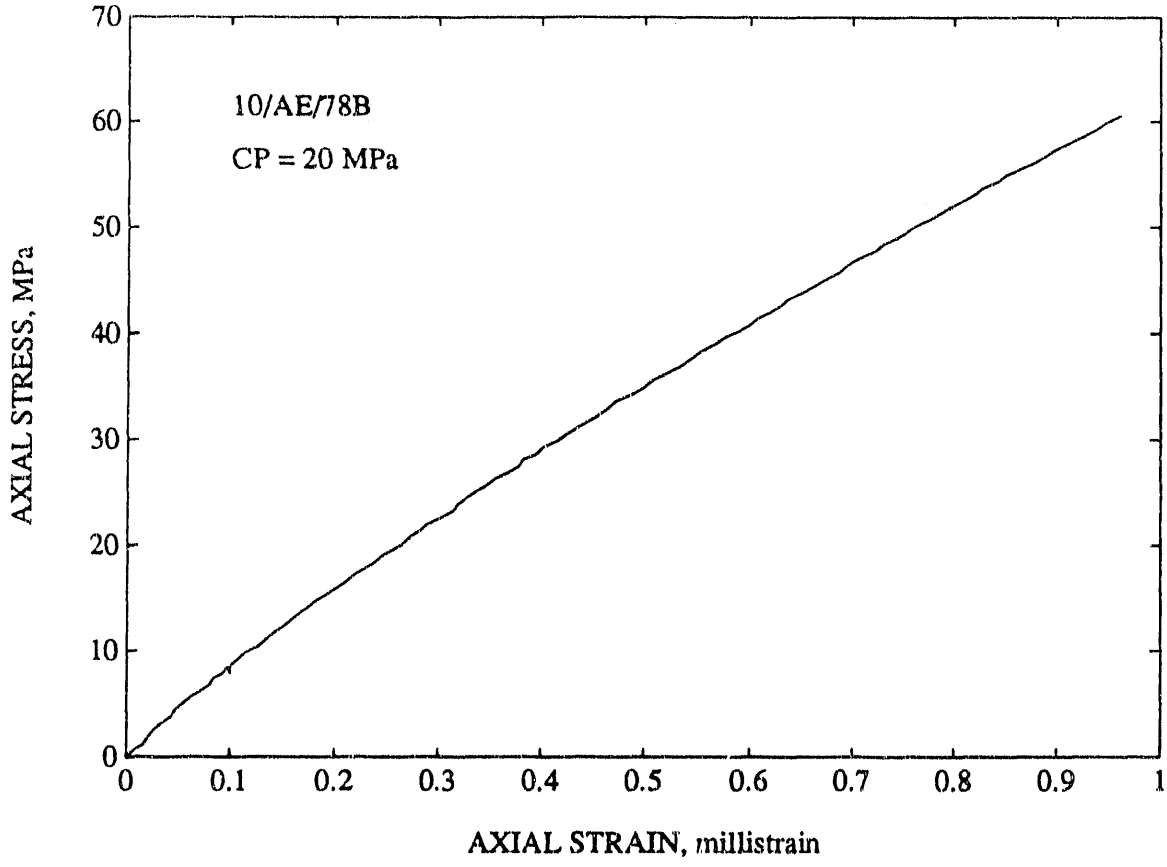

Figure 5. Axial stress is plotted as a function of axial strain for a compression experiment at a confining pressure of 20 MPa. The compression direction was normal to the layering.

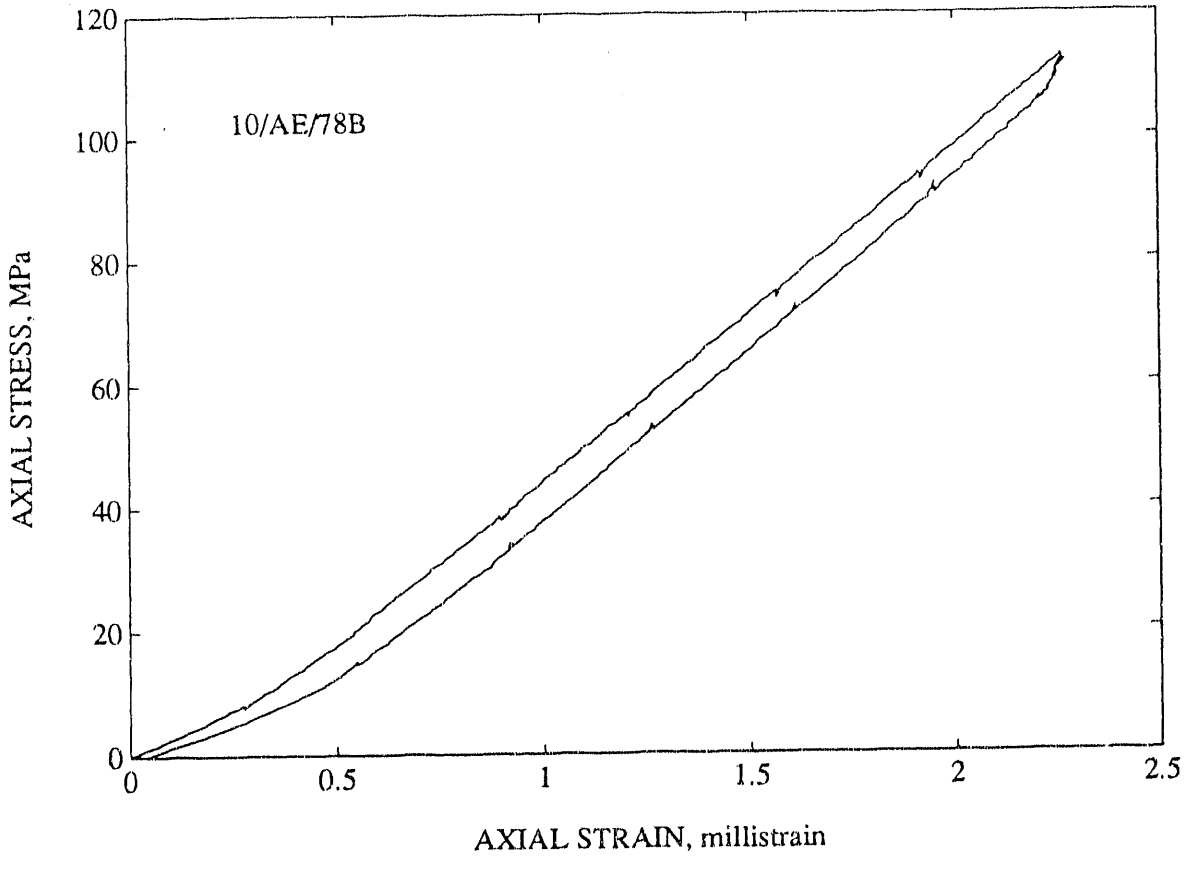

Figure 6. Axial stress is plotted as a function of axial strain for a uniaxial strain experiment. The compression direction was normal to the layering.

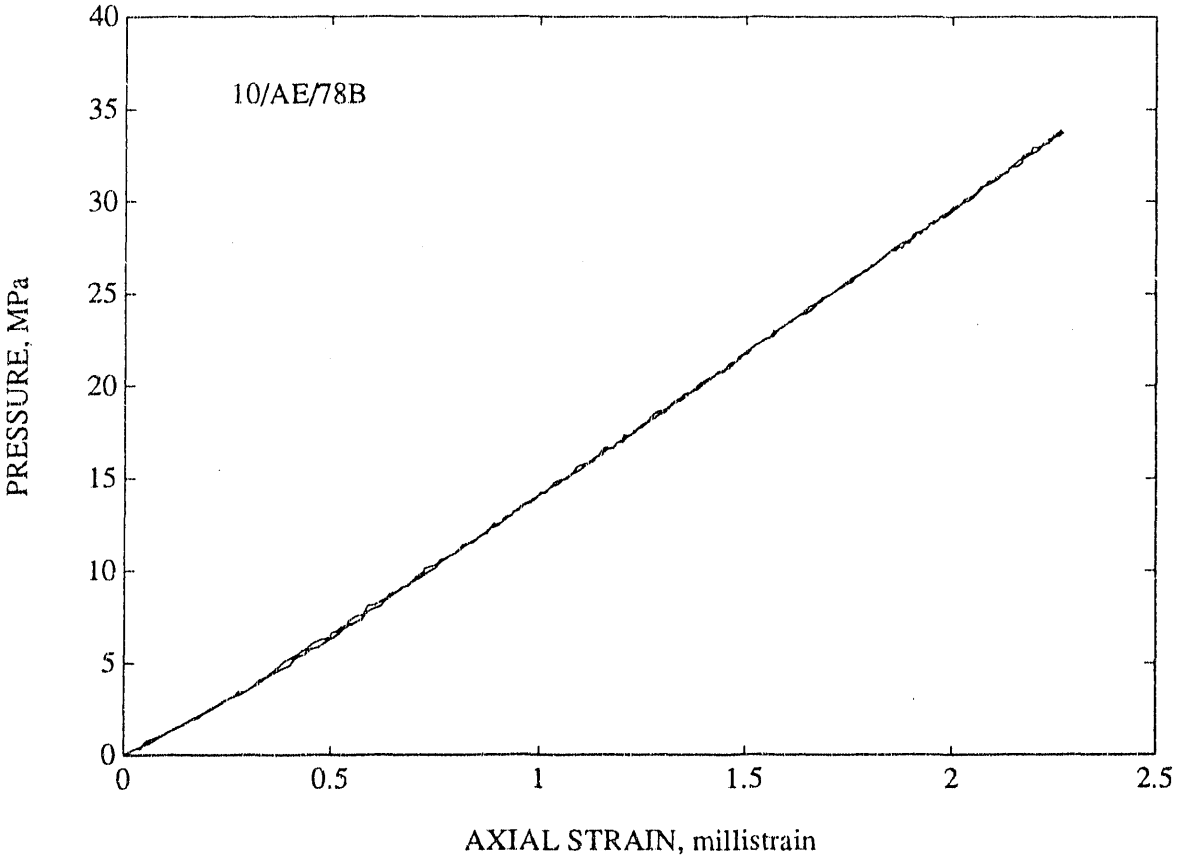

Figure 7. Confining pressure is plotted as a function of axial strain for a uniaxial strain experiment.

Appendix

Information from the Reference Information Base Used in this Report

This report contains no information from the RIB.

Candidate Information for the Reference Information Base

This report contains no candidate information for the RIB.

Candidate Information for the Site & Engineering Properties Data Base

This report contains no candidate information for the SEPDB.

DISTRIBUTION LIST

1 J. W. Bartlett, Director (RW-1)
Office of Civilian Radioactive
Waste Management
U.S. Department of Energy
1000 Independence Avenue, S.W.
Washington, DC 20585

1 F. G. Peters, Deputy Director (RW-2)
Office of Civilian Radioactive
Waste Management
U.S. Department of Energy
1000 Independence Avenue, S.W.
Washington, DC 20585

1 T. H. Isaacs (RW-4)
Office of Strategic Planning
and International Programs
Office of Civilian Radioactive
Waste Management
U.S. Department of Energy
1000 Independence Avenue, S.W.
Washington, DC 20585

1 J. D. Saltzman (RW-5)
Office of External Relations
Office of Civilian Radioactive
Waste Management
U.S. Department of Energy
1000 Independence Avenue, S.W.
Washington, DC 20585

1 Samuel Rousso (RW-10)
Office of Program and Resources
Management
Office of Civilian Radioactive
Waste Management
U.S. Department of Energy
1000 Independence Avenue, S.W.
Washington, DC 20585

1 J. C. Bresee (RW-10)
Office of Civilian Radioactive
Waste Management
U.S. Department of Energy
1000 Independence Avenue, S.W.
Washington, DC 20585

1 C. P. Gertz (RW-20)
Office of Geologic Disposal
Office of Civilian Radioactive
Waste Management
U.S. Department of Energy
1000 Independence Avenue, S.W.
Washington, DC 20585

1 S. J. Brocoum (RW-22)
Analysis and Verification Division
Office of Civilian Radioactive
Waste Management
U.S. Department of Energy
1000 Independence Avenue, S.W.
Washington, DC 20585

1 J. Roberts, Acting Assoc. Dir.
(RW-30)
Office of Systems and Compliance
Office of Civilian Radioactive
Waste Management
U.S. Department of Energy
1000 Independence Avenue, S.W.
Washington, DC 20585

1 J. Roberts (RW-33)
Director, Regulatory Compliance
Division
Office of Civilian Radioactive
Waste Management
U.S. Department of Energy
1000 Independence Avenue, S.W.
Washington, DC 20585

1 G. J. Parker (RW-332)
Office of Civilian Radioactive
Waste Management
U.S. Department of Energy
1000 Independence Avenue, S.W.
Washington, DC 20585

1 R. A. Milner (RW-40)
Office of Storage and Transportation
Office of Civilian Radioactive
Waste Management
U.S. Department of Energy
1000 Independence Avenue, S.W.
Washington, DC 20585

1 S. Rousso, Acting Assoc. Director
(RW-50)
Office of Contract Business
Management
Office of Civilian Radioactive
Waste Management
U.S. Department of Energy
1000 Independence Avenue, S.W.
Washington, DC 20585

1 Trudy Wood (RW-52)
Director, M&O Management Division
Office of Civilian Radioactive
Waste Management
U.S. Department of Energy
1000 Independence Avenue, S.W.
Washington, DC 20585

1 D. U. Deere, Chairman
Nuclear Waste Technical Review Board
1100 Wilson Blvd. #910
Arlington, VA 22209-2297

1 Dr. Clarence R. Allen
Nuclear Waste Technical Review Board
1000 E. California Blvd.
Pasadena, CA 91106

1 Dr. John E. Cantlon
Nuclear Waste Technical Review Board
1795 Bramble Dr.
East Lansing, MI 48823

1 Dr. Melvin W. Carter
Nuclear Waste Technical Review Board
4621 Ellisbury Dr., N.E.
Atlanta, GA 30332

1 Dr. Donald Langmuir
Nuclear Waste Technical Review Board
109 So. Lookout Mountain Cr.
Golden, CO 80401

1 Dr. D. Warner North
Nuclear Waste Technical Review Board
Decision Focus, Inc.
4984 El Camino Real
Los Altos, CA 94062

1 Dr. Dennis L. Price
Nuclear Wast Technical Review Board
1011 Evergreen Way
Blacksburg, VA 24060

1 Dr. Ellis D. Verink
Nuclear Waste Technical Review Board
4401 N.W. 18th Place
Gainesville, FL 32605

5 C. P. Gertz, Project Manager
Yucca Mountain Site Characterization
Project Office
U.S. Department of Energy
P.O. Box 98608--MS 523
Las Vegas, NV 89193-8608

1 C. L. West, Director
Office of External Affairs
DOE Field Office, Nevada
U.S. Department of Energy
P.O. Box 98518
Las Vegas, NV 89193-8518

12 Technical Information Officer
DOE Nevada Field Office
U.S. Department of Energy
P.O. Box 98518
Las Vegas, NV 89193-8518

1 P. K. Fitzsimmons, Technical
Advisor
Office of Assistant Manager for
Environmental Safety and Health
DOE Field Office, Nevada
U.S. Department of Energy
P.O. Box 98518
Las Vegas, NV 89193-8518

1 D. R. Elle, Director
Environmental Protection Division
DOE Nevada Field Office
U.S. Department of Energy
P.O. Box 98518
Las Vegas, NV 89193-8518

1 Repository Licensing & Quality
Assurance
Project Directorate
Division of Waste Management
U.S. Nuclear Regulatory Commission
Washington, DC 20555

1 Senior Project Manager for Yucca
Mountain
Repository Project Branch
Division of Waste Management
U.S. Nuclear Regulatory Commission
Washington, DC 20555

1 NRC Document Control Desk
Division of Waste Management
U.S. Nuclear Regulatory Commission
Washington, DC 20555

1 P. T. Prestholt
NRC Site Representative
301 E. Stewart Ave., Room 203
Las Vegas, NV 89101

1 E. P. Binnall
Field Systems Group Leader
Building 50B/4235
Lawrence Berkeley Laboratory
Berkeley, CA 94720

1 Center for Nuclear Waste
Regulatory Analyses
6220 Culebra Road
Drawer 28510
San Antonio, TX 78284

3 W. L. Clarke
Technical Project Officer for YMP
Attn: YMP/LRC
Lawrence Livermore National
Laboratory
P.O. Box 5514
Livermore, CA 94551

4 R. J. Herbst
Technical Project Officer for YMP
N-5, Mail Stop J521
Los Alamos National Laboratory
P.O. Box 1663
Los Alamos, NM 87545

1 H. N. Kalia
Exploratory Shaft Test Manager
Los Alamos National Laboratory
Mail Stop 527
101 Convention Center Dr., Suite 820
Las Vegas, NV 89109

1 J. F. Divine
Assistant Director for
Engineering Geology
U.S. Geological Survey
106 National Center
12201 Sunrise Valley Dr.
Reston, VA 22092

6 L. R. Hayes
Technical Project Officer
Yucca Mountain Project Branch--MS 425
U.S. Geological Survey
P.O. Box 25046
Denver, CO 80225

1 V. R. Schneider
Asst. Chief Hydrologist--MS 414
Office of Program Coordination
& Technical Support
U.S. Geological Survey
12201 Sunrise Valley Drive
Reston, VA 22092

1 J. S. Stuckless
Geological Division Coordinator
MS 913
Yucca Mountain Project
U.S. Geological Survey
P.O. Box 25046
Denver, CO 80225

1 D. H. Appel, Chief
Hydrologic Investigations Program
MS 421
U.S. Geological Survey
P.O. Box 25046
Denver, CO 80225

1 E. J. Helley
Branch of Western Regional Geology
MS 427
U.S. Geological Survey
345 Middlefield Road
Menlo Park, CA 94025

1 R. W. Craig, Chief
Nevada Operations Office
U.S. Geological Survey
101 Convention Center Drive
Suite 860, MS 509
Las Vegas, NV 89109

1 D. Zesiger
U.S. Geological Survey
101 Convention Center Dr.
Suite 860 - MS 509
Las Vegas, NV 89109

1 R. V. Watkins, Chief
Project Planning and Management
U.S. Geological Survey
P.O. Box 25046
421 Federal Center
Denver, CO 80225

1 A. L. Flint
U.S. Geological Survey
MS 721
P.O. Box 327
Mercury, NV 89023

1 D. A. Beck
U.S. Geological Survey
1500 E. Tropicana, Suite 201
Las Vegas, NV 89119

1 P. A. Glancy
U.S. Geological Survey
Federal Building, Room 224
Carson City, NV 89701

1 Sherman S. C. Wu
Branch of Astrogeology
U.S. Geological Survey
2255 N. Gemini Dr.
Flagstaff, AZ 86001

1 J. H. Sass
Branch of Tectonophysics
U.S. Geological Survey
2255 N. Gemini Dr.
Flagstaff, AZ 86001

1 DeWayne A. Campbell
Technical Project Officer for YMP
U.S. Bureau of Reclamation
Code D-3790
P.O. Box 25007
Denver, CO 80225

1 K. W. Causseaux
NHP Reports Chief
U.S. Geological Survey
421 Federal Center
P.O. Box 25046
Denver, CO 80225

1 W. R. Keefer
U.S. Geological Survey
913 Federal Center
P.O. Box 25046
Denver, CO 80225

1 M. D. Voegele
Technical Project Officer for YMP
Science Applications International Corp.
101 Convention Center Dr.
Suite 407
Las Vegas, NV 89109

2 L. D. Foust
Nevada Site Manager
TRW Environmental Safety Systems
101 Convention Center Drive
Suite 540, MS 423
Las Vegas, NV 89109

1 C. E. Ezra
YMP Support Project Manager
EG&G Energy Measurements, Inc.
MS V-02
P.O. Box 1912
Las Vegas, NV 89125

1 R. E. Jackson, Program Manager
Roy F. Weston, Inc.
955 L'Enfant Plaza, Southwest
Washington, DC 20024

1 Technical Information Center
Roy F. Weston, Inc.
955 L'Enfant Plaza, Southwest
Washington, DC 20024

1 D. Hedges, Vice President,
Quality Assurance
Roy F. Weston, Inc.
4425 Spring Mountain Road, Suite 300
Las Vegas, NV 89102

1 D. L. Fraser, General Manager
Reynolds Electrical & Engineering Co.
Mail Stop 555
P.O. Box 98521
Las Vegas, NV 89193-8521

1 R. F. Pritchett
Technical Project Officer for YMP
Reynolds Electrical & Engineering Co.
MS 408
P.O. Box 98521
Las Vegas, NV 89193-8521

1 B. W. Colston
President/General Manager
Las Vegas Branch
Raytheon Services Nevada
MS 416
P.O. Box 95487
Las Vegas, NV 89193-5487

1 R. L. Bullock
Technical Project Officer for YMP
Raytheon Services Nevada
Suite P250, MS 403
101 Convention Center Dr.
Las Vegas, NV 89109

1 R. E. Lowder
Technical Project Officer for YMP
MAC Technical Services
101 Convention Center Drive
Suite 1100
Las Vegas, NV 89109

1 Paul Eslinger, Manager
PASS Program
Pacific Northwest Laboratories
P.O. Box 999
Richland, WA 99352

1 A. T. Tamura
Science and Technology Division
Office of Scientific and Technical Information
U.S. Department of Energy
P.O. Box 62
Oak Ridge, TN 37831

1 Carlos G. Bell, Jr.
Professor of Civil Engineering
Civil and Mechanical Engineering Department
University of Nevada, Las Vegas
4505 South Maryland Parkway
Las Vegas, NV 89154

1 C. F. Costa, Director
Nuclear Radiation Assessment Division
U.S. Environmental Protection Agency
Environmental Monitoring Systems Laboratory
P.O. Box 93478
Las Vegas, NV 89193-3478

1 ONWI Library
Battelle Columbus Laboratory
Office of Nuclear Waste Isolation
505 King Avenue
Columbus, OH 43201

1 T. Hay, Executive Assistant
Office of the Governor
State of Nevada
Capitol Complex
Carson City, NV 89710

3 R. R. Loux, Jr.
Executive Director
Nuclear Waste Project Office
State of Nevada
Evergreen Center, Suite 252
1802 North Carson Street
Carson City, NV 89710

1 C. H. Johnson
Technical Program Manager
Nuclear Waste Project Office
State of Nevada
Evergreen Center, Suite 252
1802 North Carson Street
Carson City, NV 89710

1 John Fordham
Water Resources Center
Desert Research Institute
P.O. Box 60220
Reno, NV 89506

1 Dr. Martin Mifflin
Water Resources Center
Desert Research Institute
2505 Chandler Avenue, Suite 1
Las Vegas, NV 89120

1 Eric Anderson
Mountain West Research-Southwest Inc.
2901 N. Central Ave. #1000
Phoenix, AZ 85012-2730

1 Department of Comprehensive Planning
Clark County
225 Bridger Avenue, 7th Floor
Las Vegas, NV 89155

1 Planning Department
Nye County
P.O. Box 153
Tonopah, NV 89049

1 Lincoln County Commission
Lincoln County
P.O. Box 90
Pioche, NV 89043

5 Judy Foremaster
City of Caliente
P.O. Box 158
Caliente, NV 89008

1 Economic Development Department
City of Las Vegas
400 East Stewart Avenue
Las Vegas, NV 89101

1 Community Planning & Development
City of North Las Vegas
P.O. Box 4086
North Las Vegas, NV 89030

1 Director of Community Planning
City of Boulder City
P.O. Box 367
Boulder City, NV 89005

1 Commission of the European Communities
200 Rue de la Loi
B-1049 Brussels
BELGIUM

2 M. J. Dorsey, Librarian
YMP Research and Study Center
Reynolds Electrical & Engineering Co., Inc.
MS 407
P.O. Box 98521
Las Vegas, NV 89193-8521

1 Amy Anderson
Argonne National Laboratory
Building 362
9700 So. Cass Ave.
Argonne, IL 60439

1 Steve Bradhurst
P.O. Box 1510
Reno, NV 89505

1 Vernon Poe
P.O. Box 1026
Hawthorne, NV 89415

1 Jason Pitts
Lincoln County Courthouse
Pioche, NV 89043

1 Michael L. Baughman
35 Clark Road
Fiskdale, MA 01518

1 Glenn Van Roekel
Director of Community Development
P.O. Box 158
Caliente, NV 89008

1 Ray Williams, Jr.
P.O. Box 10
Austin, NV 89310

1 Leonard J. Fiorenzi
P.O. Box 257
Eureka, NV 89316

1 Brad Mettam
P.O. Box 539
Goldfield, NV 89013

1 Bjorn Selinder
190 W. First St.
Fallon, NV 89406

1 Charles Thistlethwaite, AICP
Associate Planner
Planning Department
Drawer L
Independence, CA 93526

10 R. J. Martin, III
New England Research, Inc.
76 Olcott Drive
White River Junction, VT 05001

1	6300	D. E. Miller
1	6302	T. E. Blejwas
1	6312	F. W. Bingham
1	6313	L. S. Costin
2	6318	R. J. Macer for 100/1232713/SAND91-0894/NQ
2	6318	F. Cheek-Martin for DRMS file 51/L02-04/06/87
1	6319	R. R. Richards
25	6115	R. H. Price
5	7141	S. A. Landenberger
8	7613-2	Document Processing for DOE/OSTI
3	7151	G. C. Claycomb
1	6115	P. J. Hommert, Acting
20	6341	WMT Library
1	6410	D. A. Dahlgren
1	8523-2	Central Technical Files

END

DATE
FILMED
9/01/92